DOI: 10.1002/ ((please add manuscript number))
Article type: Full Paper

Organic Single-Crystalline Donor-Acceptor Heterojunctions with Ambipolar Band-Like Charge Transport for Photovoltaics

Xiaoming Zhao,‡ Tianjun Liu,‡ Yuteng Zhang, Shirong Wang, Xianggao Li, Yin Xiao, Xueyan Hou, Zilu Liu, Wenda Shi and T. John S. Dennis**

X. Zhao, T. Liu, X. Hou, Dr. W. Shi, Prof. T. J. S Dennis*
School of Physics and Astronomy, Queen Mary University of London, Mile End Road, London E1 4NS, United Kingdom.
Email: j.dennis@qmul.ac.uk

Y. Zhang, Prof. S. Wang*, Prof. X. Li, Prof. Y. Xiao
School of Chemical Engineering and Technology, Tianjin University, 300072 Tianjin, China.
Email: wangshirong@tju.edu.cn

Z. Liu
School of Biological and Chemical Sciences, Queen Mary University of London, Mile End Road, London E1 4NS, United Kingdom.

X. Zhao, T. Liu, X. Hou, Z. Liu, Dr. W. Shi, Prof. T. J. S Dennis
Materials Research Institute, Queen Mary University of London, Mile End Road, London E1 4NS, United Kingdom.

Y. Zhang, Prof. S. Wang, Prof. X. Li, Prof. Y. Xiao
Collaborative Innovation Center of Chemical Science and Engineering (Tianjin), 300072 Tianjin, China.

‡ X. Zhao and T. Liu have the equivalent contribution

Keywords: Single-crystalline heterojunction; band-like; charge transport; organic photovoltaics

Abstract: Solution-processed organic single-crystalline donor-acceptor heterojunctions (SCHJs) composed of N,N,N',N'-tetraphenylbenzidine (TPB) and phenyl-C_{61}-butyric acid methyl ester ([60]PCBM) were successfully obtained and

fundamental studies on its charge transport properties were demonstrated; Revealing the advantages of applying single-crystalline heterojunctions in photovoltaic devices. The SCHJs exhibited a balanced high-mobility ambipolar charge transport with both hole and electron mobility being more than one order magnitude higher than its thin-film heterojunction (TFHJ) counterparts. The difference between single-crystalline and thin-film heterojunctions in charge transport mechanisms was revealed, and we showed that SCHJs present a more favorable band-like charge transport properties at room temperature. Organic photovoltaics fabricated on SCHJs present much higher current density and a 32-times higher *PCE* than thin-film heterojunction devices. The present work, which outlined comprehensive advantages of single-crystalline heterojunctions in charge transport properties, should accelerate the application of organic single crystals for high performance photovoltaics.

Introduction

Photovoltaic behavior of organic materials closely relates to the donor–acceptor contact mode. This is because it regulates the photocurrent generation process; which includes exciton diffusion, exciton dissociation, and charge transport.[1,2] Initially, planar heterojunctions with laminated donor and acceptor layers were found to generate photocurrents with a power conversion efficiencies (*PCE*) of around 1%.[3] A major disadvantage of these planar structures is their disorder-limited short exciton diffusion lengths below 50 nm.[4–8] To circumvent this disadvantage, a bulk heterojunction (BHJ) architecture, in which the donor and acceptor materials form three-dimensional (3D)

interpenetrating networks, was subsequently developed. BHJs better facilitates exciton dissociation,[9,10] and hence, gave a substantial improvement in *PCE* to values exceeding 10%.[11–19] Despite the success of BHJs, it remains a challenge to realize a nanoscale interpenetrating network of the donor and acceptor, such that it is consistent with the exciton diffusion length, while maintaining the required continuous transport pathways for both electrons and holes through their respective phases. This stems to some extent from a lack of direct morphological tuning, and the thermodynamic instability, of the phase domains.[20–23] Thus, the study of bulk single-crystals, by avoiding grain boundary, morphological disorder, and interfacial effects, offers a direct method of elucidating intrinsic photovoltaic properties.

Indeed, single crystals of organic semiconductors have been shown to exhibit high performances, including promising charge carrier mobility and long exciton diffusion.[24–29] In this regard, organic single crystals with ambipolar transport would be ideal candidates for high performance photovoltaic devices and for intrinsic photovoltaic studies.[30] A Single-crystalline heterojunction (SCHJ), in which single crystals of the donor and the acceptor are in contact with each other, might be expected to exhibit superior photovoltaic effects due to their highly ordered molecular packing. However, due to difficulties in achieving such a highly ordered architecture, only few pioneering studies in single crystalline donor–acceptor system has been reported in the literature; and the intrinsic photovoltaic behavior in such system remains unclear. Hu *et al.* reported the first SCHJs based organic photovoltaics (OPVs) in which copper hexadecafluorophthalocyanine (acceptor) crystal nanowires were grown onto copper

phthalocyanine (donor) crystal nanowires using physical vapor transport (PVT).[31] The resulting OPV device gave a relatively low *PCE* of 0.007%. Li *et al.* demonstrated a facile solution-grown method to fabricate consistent donor-top and acceptor-bottom single-crystalline structure through a mixed solution of C_{60} (acceptor) and 3,6-bis(5-(4-n-butylphenyl)thiophene-2-yl)-2,5-bis(2-ethylhexyl)pyrrolo[3,4-c]pyrrole-1,4-dione (donor).[32] These OPVs gave a *PCE* enhancement to 0.255%. Despite these significant progresses in SCHJs, the *PCE* of single-crystalline OPVs still remains relatively low when compared to OPVs based on thin-film heterojunctions (TFHJs) and most importantly, compared to TFHJs, the advantages of applying single-crystalline heterojunctions in photovoltaic devices have not been studied comprehensively. Therefore, in order to further enhance the *PCE*, and in order to obtain a deeper understanding of the intrinsic photovoltaic behaviors of SCHJs, fundamental studies on SCHJs are highly desirable.

Herein, we report on a solution-processed organic single-crystalline p-n heterojunction composed of two commonly-used optoelectronic materials - N,N,N',N'-tetraphenylbenzidine (TPB) and phenyl-C_{61}-butyric acid methyl ester ([60]PCBM) and demonstrate fundamental studies of its charge transport properties to reveal the significant advantages of SCHJs in photovoltaic applications. SCHJs presented here exhibit balanced ambipolar charge transport with the average performance of 0.066 cm^2 V^{-1} s^{-1} for hole mobility (μ_h) and 0.087 cm^2 V^{-1} s^{-1} for electron mobility (μ_e), respectively. Both values are more than one order magnitude higher than their thin-film heterojunction counterparts ($\mu_h = 8.3\times10^{-5}$ and $\mu_e = 5.2\times10^{-3}$ cm^2 V^{-1} s^{-1}, respectively).

To reveal the difference between single-crystalline and thin-film heterojunctions in charge transport mechanisms, temperature-dependent charge transport studies were performed at temperature ranging from 80 K to 300 K. The results show that, at room temperature, a thermally activated mechanism governs charge carrier transport in thin-film heterojunctions, while single-crystalline heterojunction present a more favorable band-like charge transport mechanism. This suggests a much lower degree of disorders presented in SCHJs and at the interface between the SCHJs and the substrates. Due to above merits, organic photovoltaics fabricated on SCHJs achieved an average *PCE* of (0.188±0.061) %, 32 times higher than devices based on thin-film heterojunction counterparts. The champion device exhibiting a *PCE* of 0.238 %, which is among the highest *PCE*s achieved on single-crystalline solar cells.

Fabrication of Single-crystalline Heterojunctions

TPB and [60]PCBM were used to grow single-crystalline donor–acceptor heterojunctions. The synthesis and purification details of TPB are included in the **Experimental Section** while its characterization including mass spectrum, ^{1}H NMR and ^{13}C NMR spectrum are shown in **Figure S1-S3** in the Supporting Information. Molecular structures of TPB and [60]PCBM are shown in **Figure 1a and b**. TPB and its derivatives are widely-used p-type semiconductors in organic electronic devices, such as organic light-emitting devices (OLEDs),[33] OFETs,[34] organic photovoltaics[35] and hybrid perovskite solar cells.[36–39] Meanwhile, [60]PCBM is the most frequently-used acceptors for organic solar cells.[40] Accordingly, TPB and [60]PCBM were selected to grow single-crystalline donor–acceptor heterojunctions in this work.

Before preparing the heterojunctions, we firstly prepared single-component crystals of TPB and [60]PCBM separately. As shown in **Figure 1c**, TPB need-like single crystals were grown by using the antisolvent vapor diffusion method[41,42] while [60]PCBM ribbon-like single crystals were obtained through liquid−liquid interfacial precipitation method[43] as indicated in **Figure 1d**. As shown in **Figure 1e and 1f,** both TPB needle crystals and [60]PCBM ribbon crystals exhibit micrometer length. The average length achieved on 50 individual crystals was (89.5 ± 37.5) μm for TPB needles and (104 ± 48.9) μm for [60]PCBM ribbons. Obtained single crystals were dispersed in tiny amount of acetone and methanol respectively to achieve a high number density of single crystals in these solvents. To fabricate TPB-bottom and [60]PCBM-up structures, TPB single crystals in acetone were drop-casting onto the substrate firstly, followed by vacuum annealing to remove the remaining solvents. Then, [60]PCBM single crystals in methanol were drop-casting onto the same substrate followed by vacuum annealing. An as-produced single-crystalline heterojunction is shown in **Figure 1h**; where [60]PCBM ribbon crystals (brown) were on top of TPB needle crystals (light blue).

Morphology and Crystal Structures

After obtaining the single-component crystals and single-crystalline heterojunctions, the morphologies were characterized by scanning electron microscopy (SEM) and atomic force microscopy (AFM) as shown in **Figure 2a** and **Figure S4** in the supporting information. The width and thickness for TPB needle crystals are (392±107) nm and (88.3±14.2) nm, respectively. [60]PCBM ribbon crystals present two-dimensional nano-structures with the width of (19.4±7.53) μm and the thickness

of (184±34.6) nm. In order to characterize the chemical composition of the overlapping bilayer, the crystals were examined with energy dispersive spectrum (EDS) on SEM as shown in **Figure 2c**. Element mapping of O ([60]PCBM) and N (TPB) clearly showed that the ribbon is the single crystal of [60]PCBM while the needle is the single crystal of TPB. The [60]PCBM ribbon is on top of TPB needle to form single-crystalline heterojunction. From the AFM measurements shown in **Figure 2b** and **Figure S5** (Supporting Information), the thickness of the overlapping p-n junction was found to be 275 nm, consisting of 84 nm of TPB and 191 nm of [60]PCBM.

The crystal structures of the single-component crystals and single-crystalline heterojunctions were studied by select area electron diffraction (SAED) on transmission electron microscopy (TEM) and x-ray diffraction (XRD). TEM images in **Figure 2c and d** reveal the uniformity of both the TPB needle crystals and [60]PCBM ribbon crystals. The presence of discrete diffraction points, and no change in the SAED patterns (**inset of Figure 2c and d**), are observed for different parts of the same single crystals. This indicates the single crystallinity of these two materials. Deeper insight into the molecular organization was obtained by XRD as shown in **Figure 2e**. The XRD pattern of TPB can be indexed with a monoclinic crystal system with cell dimensions of a = 9.68 Å, b = 14.19 Å, c = 9.73 Å, which is consistent with a previous report.[44] For the [60]PCBM ribbon crystals, the XRD pattern can be indexed with a solvent-free monoclinic crystal system with cell dimensions of a = 13.36 Å, b = 15.58 Å, c = 19.50 Å, which coincides well with a report in the literature.[45] The XRD pattern of crystal heterojunctions showed combined diffraction peaks of both TPB and [60]PCBM single

crystals, indicating the presence of these two different single crystals. Therefore, the SEM, EDS, AFM, TEM, SAED and XRD evidences demonstrate that we indeed obtained the single-crystalline p-n heterojunctions of TPB needle and [60]PCBM ribbon crystals.

Ambipolar Charge Transport Properties

The single-crystalline nature of our p-n heterojunction indicates their high quality and potential use in studying their intrinsic behaviors in organic photovoltaics. Due to the minimized molecular disorder and defects, organic single crystals usually have a high charge mobility, which is especially needed in organic photovoltaic device to reduce the recombination of charge carriers.[46–49] To study the ambipolar charge transport, we artificially designed an asymmetric organic field-effect transistors (OFETs) structure with a bottom-gate and top-contact configuration. **Figure 3a and b** respectively show the schematic diagram and the SEM images of the final device. When Source 1 and Drain 2 (or Source 2 and Drain 1) were used as source/drain electrode pair, the charge transport through single-crystalline heterojunction will dominate the device performance. Here, we used Source 2 and Drain 1 as the electrode pair. The typical transfer characteristics of devices are shown in **Figure 3c and d**, exhibiting classic V-shaped curves, wherein the two arms correspond to electron transport and hole transport, indicative of the ambipolar charge transport in single-crystalline p-n heterojunction. The output characteristics in p-channel (**Figure S6**) and n-channel (**Figure S7**) operation channel operation modes confirmed the excellent gate modulation. The best charge transport performance achieved from a single-crystalline

p-n heterojunction was a balanced hole and electron mobility of 0.08 $cm^2\ V^{-1}\ s^{-1}$ and 0.11 $cm^2\ V^{-1}\ s^{-1}$, respectively. The histograms of hole and electron mobility obtained from 50 devices based on p-n junctions are shown in **Figure S8** and **Figure S9**. For hole transport, an average hole mobility (μ_h) of (0.066 ± 0.030) $cm^2\ V^{-1}\ s^{-1}$ (range: 0.029 – 0.098), on-to-off current ratio (I_{on}/I_{off}) > 10^3, and threshold voltage (V_T) between -31.3 and -43.2 V were obtained. For electron transport, we achieved an average electron mobility (μ_e) of (0.087 ± 0.026) $cm^2\ V^{-1}\ s^{-1}$ (range: 0.043 – 0.129), I_{on}/I_{off} > 10^3, and V_T between 29.5 and 47.3 V. For comparison, charge transport properties of thin-film heterojunctions of TPB and [60]PCBM were also studied as shown in **Figure 3e and f**. With 50 devices tested, average μ_h of (8.3 ± 2.5×10^{-5}) $cm^2\ V^{-1}\ s^{-1}$ (range: 3.9–12.3×10^{-5}, **Figure S10**), I_{on}/I_{off} > 10^2, and V_T between -10.3 and -45.8 V were obtained. For electron transport in thin-film heterojunction, average μ_e of (5.2±1.3×10^{-3}) $cm^2\ V^{-1}\ s^{-1}$ (range: 2.7–7.2×10^{-3}, **Figure S11**), I_{on}/I_{off} > 10, and V_T between 23.5 and 51.7 V were achieved. This comparison clearly shows the much better charge transport properties of single-crystalline heterojunction, whereby both hole and electron mobility were more than one order magnitude higher than those of their thin-film heterojunction counterparts. In addition, the electron and hole mobility in thin-film heterojunction is considerably unbalanced with a two-order magnitude difference; while for our single-crystalline heterojunction, the electron and hole mobility is much more balanced.

To compare the quality of interface between TPB and [60]PCBM in SCHJ and TFHJ, subthreshold swing (*S.S.*) and interface trap density (N_{SS}), which represent the

interface quality and the trap behavior in OFETs, were calculated according to the Equation (1) and Equation (2):[50]

$$S.S. = \frac{dV_{GS}}{dI_{DS}} \quad (1)$$

$$N_{ss} = \left[\frac{S\log(e)}{kT/q} - 1\right]\frac{C_i}{q} \quad (2)$$

Where C_i is the capacitance per unit area; k is Boltzmann's constant, and T is the absolute temperature, I_{DS} is the drain–source current, V_{GS} is the gate voltage. OFETs based on SCHJs have the subthreshold swing of 8.42 V decade^{-1} and interface trap density of 9.68×10^{12} cm^{-2} eV^{-1}, which is much lower compared to the devices based on TFHJs (*S.S.* = 33.91 V decade^{-1}, N_{SS} = 51.43×10^{12} cm^{-2} eV^{-1}). This further confirmed that SCHJ provides the devices with minimal interface defects and thus result in higher device performances. These excellent features of single-crystalline heterojunction are attributed reduced charge carrier recombination, which enhanced the performance of the organic photovoltaics.[46–48]

Charge Transport Mechanisms

To compare the charge transport mechanisms in single-crystalline and thin-film p-n heterojunctions, temperature-dependent ambipolar mobility were tested in a vacuum holder by cooling the samples from 300 to 80 K. The hole and electron mobility were measured every 10 K. Interestingly, as shown in the **Figure 4e**, the hole and electron mobility in the single-crystalline heterojunction exhibits an increase-at-first-and-then-decrease behavior on cooling the samples; whereas for thin-film heterojunction, both the electron and hole mobility decrease monotonically with decreasing temperature. For

the single-crystalline heterojunction, the transition temperatures between the different temperature-dependent behavioral regions was 240 K for electron transport and 270 K for hole transport. **Figure 4a and b** shows the p-channel operation mode OFET transfer curves of single-crystalline heterojunctions at the temperature from 300 K to 90 K with the square root of drain current plotted against the gate voltage. In the low-temperature region (90 K – 270 K, **Figure 4a**), the hole mobility decreased by cooling the samples, yielding a positive mobility temperature coefficient ($d\mu/dT > 0$). For n-channel operation mode OFETs based on single-crystalline heterojunctions, a similar trend was observed with a transition temperature at 240 K (**Figure 4c**). Such behavior is commonly observed in organic field effect transistors,[51–54] reflecting the gate voltage filling up low-mobility trap states.[55] This implies that a thermally activated mechanism governs both the hole and electron transport in the single-crystalline heterojunctions at low temperature regions. In low temperature regions, most charge carriers are trapped in localized shallow traps formed by chemical impurities, sites of structural disorder, and surface states, and then charge transport occurs through extended states (transport level) when the carriers are thermally activated (released) from the traps. Fitting the data with Equation (3),[56]

$$\mu = \mu_0 \exp\left(\frac{-E_a}{k_B T}\right) \qquad (3)$$

where E_a is the activation energy and k_B is the Boltzmann constant, leads to activation energies of 19.6 meV for hole transport and 12.4 meV for electron transport, as shown in **Figure 4f**. The relevant lower activation energies of single-crystalline

heterojunction here suggest a low degree of disorders presented in the single-crystalline heterojunctions and at the interface between the semiconductors and the substrates.

On the other hand, in the high-temperature region (270 – 300 K for hole transport and 240 - 300 K for electron transport), the mobility exhibits a negative mobility temperature coefficient ($d\mu/dT < 0$). The hole (electron) mobility of single-crystalline heterojunctions increases monotonically upon cooling the samples from 300 to 270 K (300 to 240 K). The observation of the negative mobility temperature coefficients is a general signature of charge carrier delocalization over a few molecules, which is the band-like transport.[56,57] In the high-temperature region, sufficient thermal energy is available such that the influence of trapping could be eliminated and the overall conduction was determined by the intrinsic transport through the extended transport level within the single crystals. Band-like temperature dependence is the signature of high-quality crystals and excellent electrical conduction.[51]

However, for the thin-film heterojunction counterparts, both the electron and hole mobility decrease monotonically by cooling the samples at the whole temperature region, without any favorable band-like charge transport property, which led to a relatively higher activation energies of 106 meV for hole transport and 80 meV for electron transport (**Figure 4f**).

The relatively high-mobility balanced ambipolar charge transport property, highly-efficient band-like charge transport at room temperature, together with the excellent electrical conduction, endows the single-crystalline donor–acceptor

heterojunctions a promising replacement of thin-film heterojunctions with the potential ability to generate higher-density photocurrents.

Photovoltaic Properties

Unlike traditional photovoltaic systems, our devices fabricated in a planar configuration in which the segregated donor and acceptor layers within the single-crystalline heterojunction, which functioned as charge transport channels, were parallel to the substrates.[31] As the active areas of single-crystalline p-n heterojunctions are quite smaller compared to their thin-film counterparts, we employed cooper grids to shadow mask the active areas when evaporating metal electrodes (Al). **Figure 5a, b and c** shows a schematic diagram, SEM images, and energy level alignment of the device configuration. Samples were measured under ambient conditions by a probe station equipped with a solar simulator with an AM1.5G filter at an intensity of 100 mW cm^{-2}. A clear photovoltaic effect was observed for photovoltaic devices based on single-crystal TPB-PCBM heterojunctions. A total of 32 devices were tested, which gave the *PCE* values shown in **Figure 5f**. An average *PCE* of (0.188 ± 0.061) % was obtained for single-crystalline OPV devices. A champion photovoltaic cell with an open-circuit voltage (V_{OC}) of 0.530 V, a short-circuit current density (J_{SC}) of 1.152 mA cm^{-2} and a fill factor (*FF*) of 0.390, which corresponded to an overall *PCE* of 0.238% was achieved as shown in **Figure 5c**. Note that our devices have a planar 2D geometry, and the direction of current flow is perpendicular to the light, which is different from the traditional sandwich thin film OPV devices. Here, the contacting area between device and light was chosen for the calculation of photocurrent densities. In order to

confirm the photocurrent was truly generated by the p-n heterojunctions, rather than the Schottky contacts[58–60] between single-component crystals and electrodes, individual TPB or [60]PCBM single crystal devices were fabricated by the same procedure mentioned before and tested under the same conditions. However, no photovoltaic effects were detected as shown in **Figure S12 and S13**. This suggested that the photocurrent generation was indeed attributable to a single-crystalline p–n junctions.

For comparison, devices with a bilayer heterojunction structure of TPB (~50 nm) and [60]PCBM (~50 nm) were also fabricated. Photovoltaic measurements were tested under the same conditions mentioned above. However, very weak photovoltaic effect with a quite low maximum *PCE* of only 0.00835% was observed as shown in **Figure 5c**. In this condition, a total of 32 devices were tested with the *PCE* values shown in **Figure 5g**. The evergy *PCE* is only (0.00580±0.00117) %, 32 times lower than that of the single-crystalline heterojunction system. It is worth noting that the J_{SC} of single-crystalline devices is much higher than thin-film devices, which further confirms that the single-crystalline donor–acceptor heterojunctions generate a much higher-density photocurrent. These results clearly demonstrate that the highly ordered single-crystalline p–n heterojunction can substantially improve the photovoltaic properties, indicating that this system has great potential in the photovoltaic field.

Further improvement may be achieved by increasing the light absorption and modifying the electrodes to achieve better electronic contact. In particular, the very weak light absorption of the present donor TPB hinders the high-efficient exciton generation and diffusion and thus reduce the device performance. Single crystals of

high-absorption donors or inserted absorber materials (such as perovskite absorbers) are desired.

Conclusions

In conclusion, solution-processed organic single-crystalline p-n heterojunctions composed of TPB and [60]PCBM were successfully achieved and fundamental studies of its charge transport properties were demonstrated. The SCHJs exhibited a balanced high-mobility ambipolar charge transport with both hole and electron mobility being more than one order magnitude higher than its thin-film heterojunction counterparts. We revealed the difference between single-crystalline and thin-film heterojunctions in charge transport mechanisms and showed that SCHJs present a more favorable band-like charge transport properties at room temperature. Organic photovoltaics fabricated on SCHJs present much higher current density and a 32-times higher *PCE* than current TFHJs devices. The champion device exhibiting a *PCE* of 0.24 %, which is among the highest *PCEs* achieved on solar cells based on organic single-crystalline heterojunctions. By selecting high-absorption donors and optimizing the device structure, the device performance should be further improved. The present work, which outlined comprehensive advantages of single-crystalline heterojunctions in OPVs, should accelerate the application of organic single crystals for high performance photovoltaics.

Supporting Information

Supporting Information is available from the Wiley Online Library or from the author.

Acknowledgements

X. Zhao, T. Liu, X. Hou and Z. Liu thank the China Scholarship Council for funding.

Notes

The authors declare no competing financial interest.

Received: ((will be filled in by the editorial staff))

Revised: ((will be filled in by the editorial staff))

Published online: ((will be filled in by the editorial staff))

[1] Y. Lin, Y. Li, X. Zhan, *Chem. Soc. Rev.* **2012**, *41*, 4245.

[2] A. J. Heeger, *Chem. Soc. Rev.* **2010**, *39*, 2354.

[3] C. W. Tang, *Appl. Phys. Lett.* **1986**, *48*, 183.

[4] P. Peumans, A. Yakimov, S. R. Forrest, *J. Appl. Phys.* **2003**, *93*, 3693.

[5] R. R. Lunt, N. C. Giebink, A. A. Belak, J. B. Benziger, S. R. Forrest, *J. Appl. Phys.* **2009**, *105*, DOI 10.1063/1.3079797.

[6] D. E. Markov, E. Amsterdam, P. W. M. Blom, A. B. Sieval, J. C. Hummelen, *J. Phys. Chem. A* **2005**, *109*, 5266.

[7] P. E. Shaw, A. Ruseckas, I. D. W. Samuel, *Adv. Mater.* **2008**, *20*, 3516.

[8] W. A. Luhman, R. J. Holmes, *Adv. Funct. Mater.* **2011**, *21*, 764.

[9] G. Yu, J. Gao, J. C. Hummelen, F. Wudl, A. J. Heeger, *Science (80-.).* **1995**, *270*, 1789.

[10] J. J. M. Halls, C. A. Walsh, N. C. Greenham, E. A. Marseglia, R. H. Friend, S. C. Moratti, A. B. Holmes, *Nature* **1995**, *376*, 498.

[11] T. K. Mullenbach, K. A. McGarry, W. A. Luhman, C. J. Douglas, R. J. Holmes, *Adv. Mater.* **2013**, *25*, 3689.

[12] L. Dou, J. You, Z. Hong, Z. Xu, G. Li, R. A. Street, Y. Yang, *Adv. Mater.* **2013**, *25*, 6642.

[13] J. You, L. Dou, K. Yoshimura, T. Kato, K. Ohya, T. Moriarty, K. Emery, C. C. Chen, J. Gao, G. Li, Y. Yang, *Nat. Commun.* **2013**, *4*, DOI 10.1038/ncomms2411.

[14] Z. He, C. Zhong, S. Su, M. Xu, H. Wu, Y. Cao, A. K. K. A. Kyaw, D. D. H. Wang, V. Gupta, J. Zhang, S. Chand, G. C. Bazan, A. J. Heeger, *Nat. Photonics* **2013**, *25*, 593.

[15] J. Zhou, Y. Zuo, X. Wan, G. Long, Q. Zhang, W. Ni, Y. Liu, Z. Li, G. He, C. Li, B. Kan, M. Li, Y. Chen, *J. Am. Chem. Soc.* **2013**, *135*, 8484.

[16] S. H. Liao, H. J. Jhuo, Y. S. Cheng, S. A. Chen, *Adv. Mater.* **2013**, *25*, 4766.

[17] W. Li, A. Furlan, K. H. Hendriks, M. M. Wienk, R. A. J. Janssen, *J. Am. Chem. Soc.* **2013**, *135*, 5529.

[18] K. Li, Z. Li, K. Feng, X. Xu, L. Wang, Q. Peng, *J. Am. Chem. Soc.* **2013**, *135*, 13549.

[19] W. Cao, J. Xue, *Energy Environ. Sci.* **2014**, *7*, 2123.

[20] B. C. Thompson, J. M. J. Fréchet, *Angew. Chemie - Int. Ed.* **2008**, *47*, 58.

[21] H. Hoppe, N. S. Sariciftci, *J. Mater. Chem.* **2006**, *16*, 45.

[22] M. Jørgensen, K. Norrman, F. C. Krebs, *Sol. Energy Mater. Sol. Cells* **2008**, *92*, 686.

[23] G. Dennler, M. C. Scharber, C. J. Brabec, *Adv. Mater.* **2009**, *21*, 1323.

[24] V. Podzorov, *MRS Bull.* **2013**, *38*, 15.

[25] R. Li, W. Hu, Y. Liu, D. Zhu, *Acc. Chem. Res.* **2010**, *43*, 529.

[26] C. Reese, Z. Bao, *Mater. Today* **2007**, *10*, 20.

[27] J. H. Oh, H. W. Lee, S. Mannsfeld, R. M. Stoltenberg, E. Jung, Y. W. Jin, J. M. Kim, J.-B. Yoo, Z. Bao, *Proc. Natl. Acad. Sci.* **2009**, *106*, 6065.

[28] W. Jiang, Y. Zhou, H. Geng, S. Jiang, S. Yan, W. Hu, Z. Wang, Z. Shuai, J. Pei, *J. Am. Chem. Soc.* **2011**, *133*, 1.

[29] X. ZHAO, T. Liu, Y. Cui, X. HOU, Z. Liu, X. Dai, J. Kong, W. SHI, T. J. S. Dennis, *Nanoscale* **2018**, DOI: 10.1039/C8NR01305E.

[30] G. M. Akselrod, P. B. Deotare, N. J. Thompson, J. Lee, W. A. Tisdale, M. A. Baldo, V. M. Menon, V. Bulović, *Nat. Commun.* **2014**, *5*, 3646.

[31] Y. Zhang, H. Dong, Q. Tang, S. Ferdous, F. Liu, S. C. B. Mannsfeld, W. Hu, A. L. Briseno, *J. Am. Chem. Soc.* **2010**, *132*, 11580.

[32] H. Li, C. Fan, W. Fu, H. L. Xin, H. Chen, *Angew. Chemie - Int. Ed.* **2015**, *54*, 956.

[33] X. Zhao, S. Wang, J. You, Y. Zhang, X. Li, *J. Mater. Chem. C* **2015**, *3*, 11377.

[34] T. P. I. Saragi, T. Fuhrmann-Lieker, J. Salbeck, *Adv. Funct. Mater.* **2006**, *16*, 966.

[35] T. Osasa, S. Yamamoto, M. Matsumura, *Adv. Funct. Mater.* **2007**, *17*, 2937.

[36] F. Zhang, X. Zhao, C. Yi, D. Bi, X. Bi, P. Wei, X. Liu, S. Wang, X. Li, S. M. Zakeeruddin, M. Grätzel, *Dye. Pigment.* **2017**, *136*, 273.

[37] X. Zhao, F. Zhang, C. Yi, D. Bi, X. Bi, P. Wei, J. Luo, X. Liu, S. Wang, X. Li, S. M. Zakeeruddin, M. Grätzel, *J. Mater. Chem. A* **2016**, *4*, 16330.

[38] P. Qi, F. Zhang, X. Zhao, X. Liu, X. Bi, P. Wei, Y. Xiao, X. Li, S. Wang, *Energy Technol.* **2017**, *5*, 1173.

[39] W. Shi, X. Hou, T. Liu, X. Zhao, A. B. Sieval, J. C. Hummelen, T. J. S. Dennis, *Chem. Commun.* **2017**, *53*, 975.

[40] F. Zhang, W. Shi, J. Luo, N. Pellet, C. Yi, X. Li, X. Zhao, T. J. S. Dennis, X. Li, S. Wang, Y. Xiao, S. M. Zakeeruddin, D. Bi, M. Grätzel, *Adv. Mater.* **2017**, *29*, DOI 10.1002/adma.201606806.

[41] D. Shi, X. Qin, Y. Li, Y. He, C. Zhong, J. Pan, H. Dong, W. Xu, T. Li, W. Hu, J. L. Brédas, O. M. Bakr, *Sci. Adv.* **2016**, *2*, e1501491.

[42] D. Shi, V. Adinolfi, R. Comin, M. Yuan, E. Alarousu, A. Buin, Y. Chen, S. Hoogland, A. Rothenberger, K. Katsiev, Y. Losovyj, X. Zhang, P. A. Dowben, O. F. Mohammed, E. H. Sargent, O. M. Bakr, *Science (80-.).* **2015**, *347*, 519.

[43] L. Zheng, Y. Han, *J. Phys. Chem. B* **2012**, *116*, 1598.

[44] X. Shao, K. Asahi, T. Yamauchi, T. Sugimoto, M. Shiro, *Acta Crystallogr. Sect. E Struct. Reports Online* **2009**, *65*, DOI 10.1107/S1600536809016389.

[45] G. Paternò, A. J. Warren, J. Spencer, G. Evans, V. G. Sakai, J. Blumberger, F. Cacialli, *J. Mater. Chem. C* **2013**, *1*, 5619.

[46] P. Vanlaeke, A. Swinnen, I. Haeldermans, G. Vanhoyland, T. Aernouts, D. Cheyns, C. Deibel, J. D'Haen, P. Heremans, J. Poortmans, J. V. Manca, *Sol. Energy Mater. Sol. Cells* **2006**, *90*, 2150.

[47] D. Chen, A. Nakahara, D. Wei, D. Nordlund, T. P. Russell, *Nano Lett.* **2011**, *11*, 561.

[48] H. Zhang, L. Jiang, Y. Zhen, J. Zhang, G. Han, X. Zhang, X. Fu, Y. Yi, W. Xu, H. Dong, *Adv. Electron. Mater.* **2016**, *2*.

[49] M. Morana, P. Koers, C. Waldauf, M. Koppe, D. Muehlbacher, P. Denk, M. Scharber, D. Waller, C. Brabec, *Adv. Funct. Mater.* **2007**, *17*, 3274.

[50] L. S. Tsai, C. H. Wang, W. Y. Chen, W. C. Wang, J. Hwang, *Org. Electron. physics, Mater. Appl.* **2010**, *11*, 123.

[51] N. A. Minder, S. Ono, Z. Chen, A. Facchetti, A. F. Morpurgo, *Adv. Mater.* **2012**, *24*, 503.

[52] B. J. Kim, H. Yu, J. H. Oh, M. S. Kang, J. H. Cho, *J. Phys. Chem. C* **2013**, *117*, 10743.

[53] N. A. Minder, S. Lu, S. Fratini, S. Ciuchi, A. Facchetti, A. F. Morpurgo, *Adv. Mater.* **2014**, *26*, 1254.

[54] Y. Krupskaya, M. Gibertini, N. Marzari, A. F. Morpurgo, *Adv. Mater.* **2015**, *27*, 2453.

[55] X. Xu, Y. Yao, B. Shan, X. Gu, D. Liu, J. Liu, J. Xu, N. Zhao, W. Hu, Q. Miao, *Adv. Mater.* **2016**, *28*, 5276.

[56] T. Sakanoue, H. Sirringhaus, *Nat. Mater.* **2010**, *9*, 736.

[57] C. Liu, T. Minari, X. Lu, A. Kumatani, K. Takimiya, K. Tsukagoshi, *Adv. Mater.* **2011**, *23*, 523.

[58] D. L. Morel, A. K. Ghosh, T. Feng, E. L. Stogryn, P. E. Purwin, R. F. Shaw, C. Fishman, *Appl. Phys. Lett.* **1978**, *32*, 495.

[59] G. A. Chamberlain, P. J. Cooney, S. Dennison, *Nature* **1981**, *289*, 45.

[60] S. Karak, J. A. Lim, S. Ferdous, V. V. Duzhko, A. L. Briseno, *Adv. Funct. Mater.* **2014**, *24*, 1039.

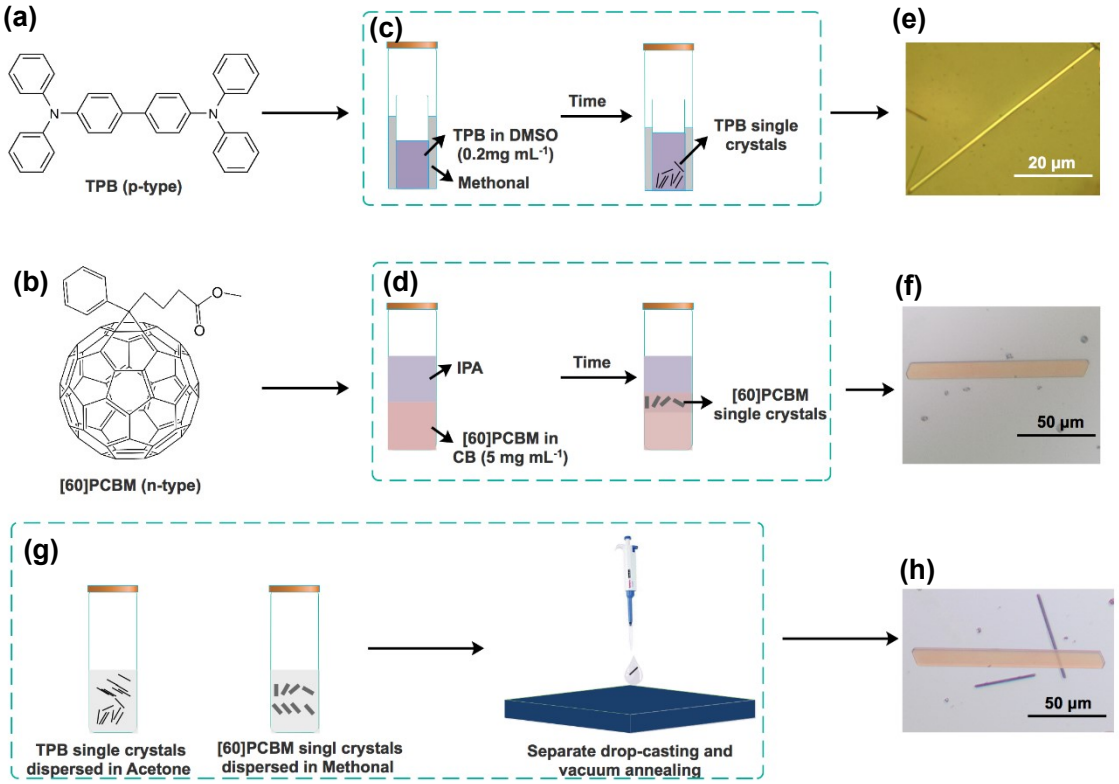

Figure 1 Molecular structures of (a) TPB and (b) [60]PCBM; (c)Schematic diagram of TPB single crystals growth by antisolvent vapor diffusion method; (d) Schematic diagram of [60]PCBM single crystals growth by liquid−liquid interfacial precipitation method; (e) Schematic diagram of the fabrication of TPB-[60]PCBM single-crystalline heterojunctions; Optical microscope images of (f) TPB single crystals, (g) [60]PCBM single crystals and (h) single-crystalline TPB-[60]PCBM heterojunction.

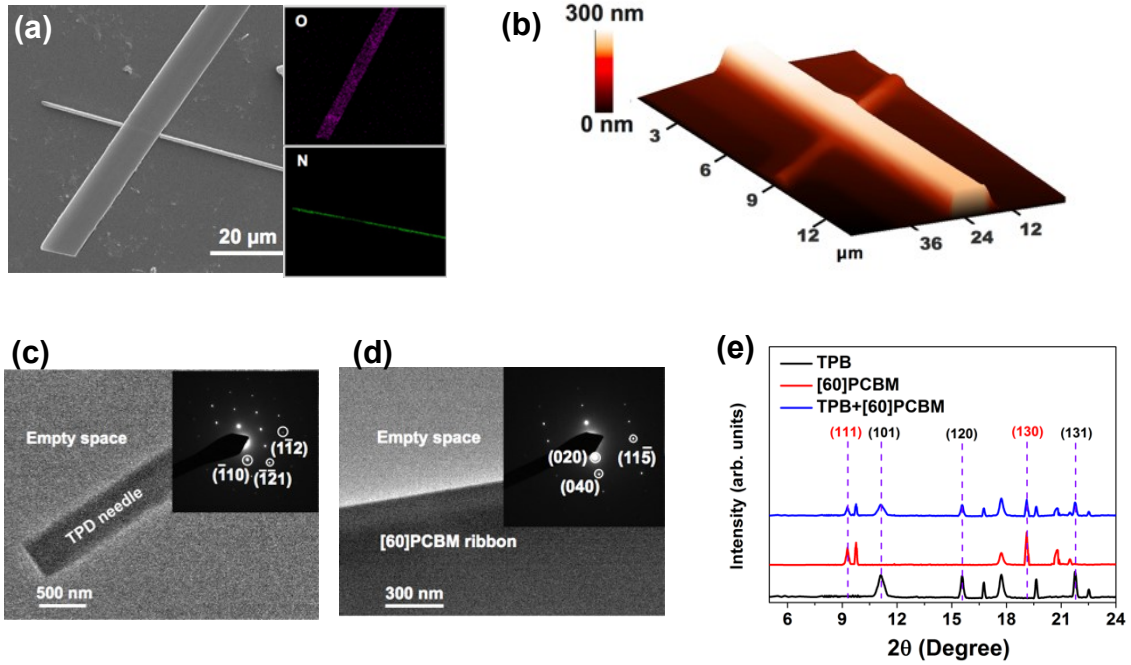

Figure 2 SEM images of (a) single-crystalline p-n heterojunction (inset: element mapping of O and N using EDS on SEM); (b) AFM 3D images of single-crystalline p-n heterojunction; TEM images of (c) TPB single crystals and (d) [60]PCBM single crystals (inset: SAED patterns) (e) XRD patterns for individual single crystals and crystal heterojunctions.

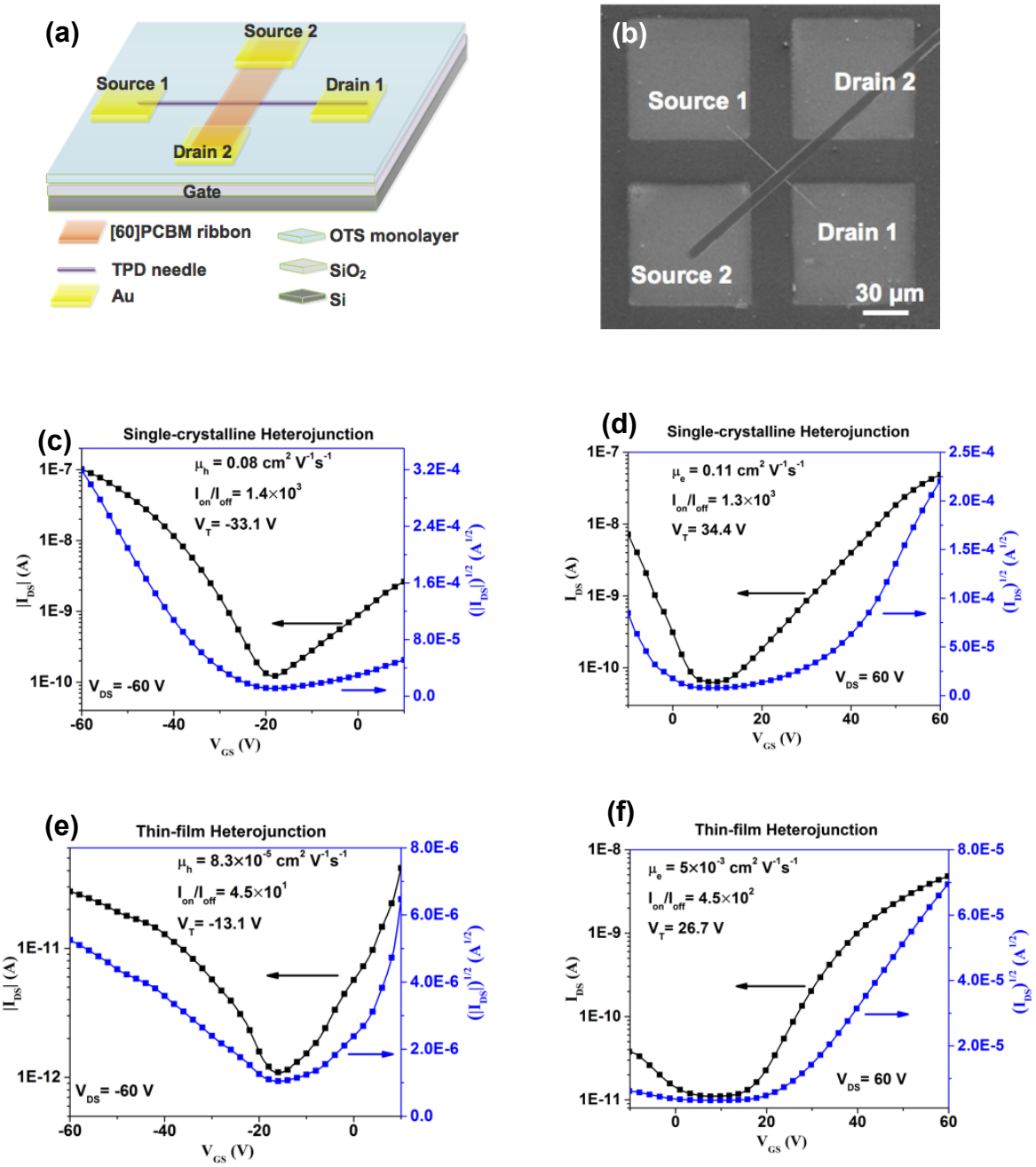

Figure 3 (a) Schematic diagram and (b) SEM image of device structure based on single-crystalline heterojunction; Typical transfer characteristics of (c) single-crystalline device and (e) thin-film device in p-channel operation mode under negative drain bias; Typical transfer characteristics of (d) single-crystalline device and (f) thin-film device in p-channel operation mode under negative drain bias.

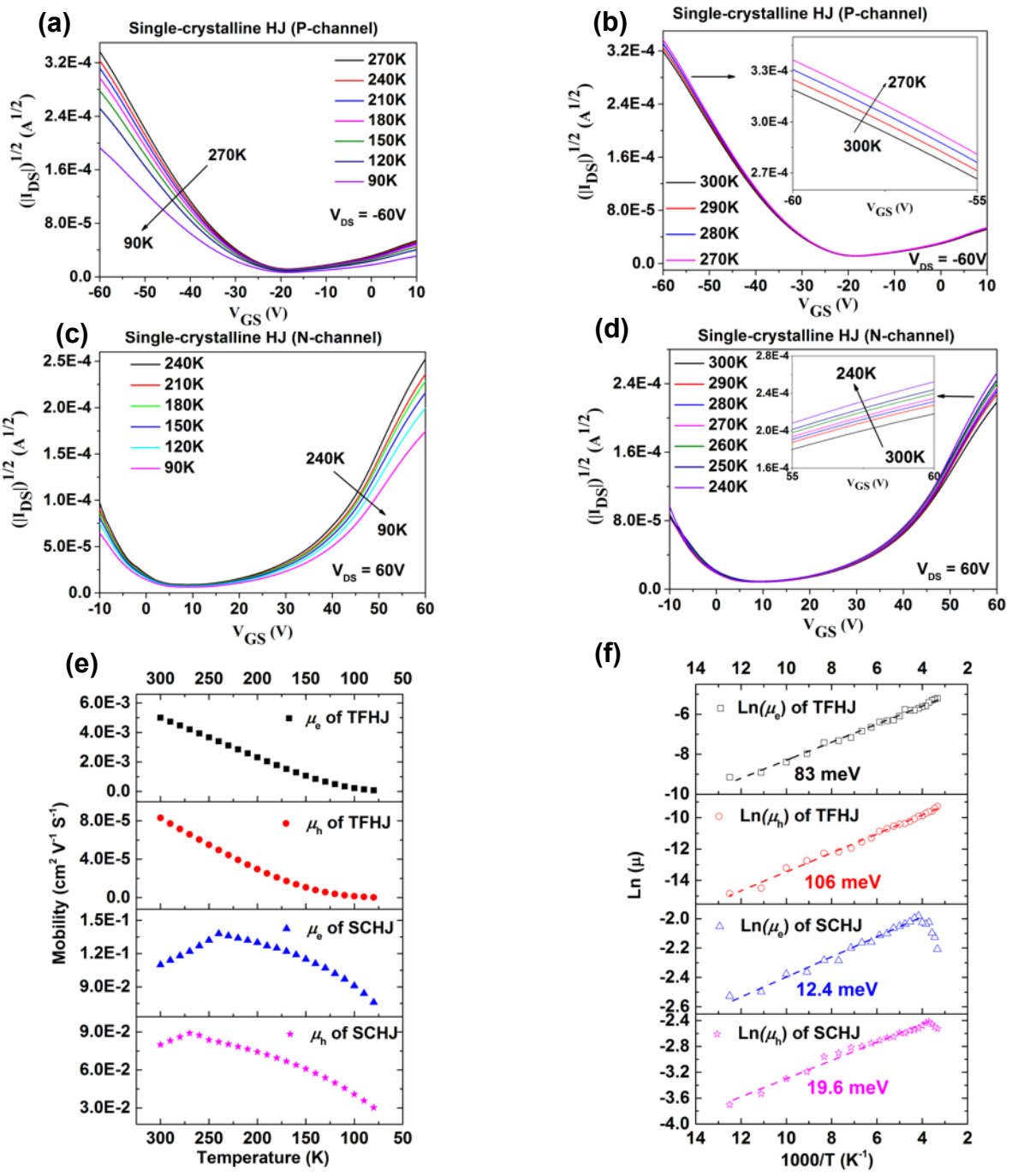

Figure 4 Transfer characteristics of single-crystalline device in p-channel operation mode at the temperature from (a) 300K to 270K and (b) 270K to 90K; Transfer characteristics of single-crystalline device in n-channel operation mode at the temperature from (a) 300K to 240K and (b) 240K to 90K; (e) Temperature dependence of mobility and (f) Ln(μ) versus $1/T$ for the two kinds of devices.

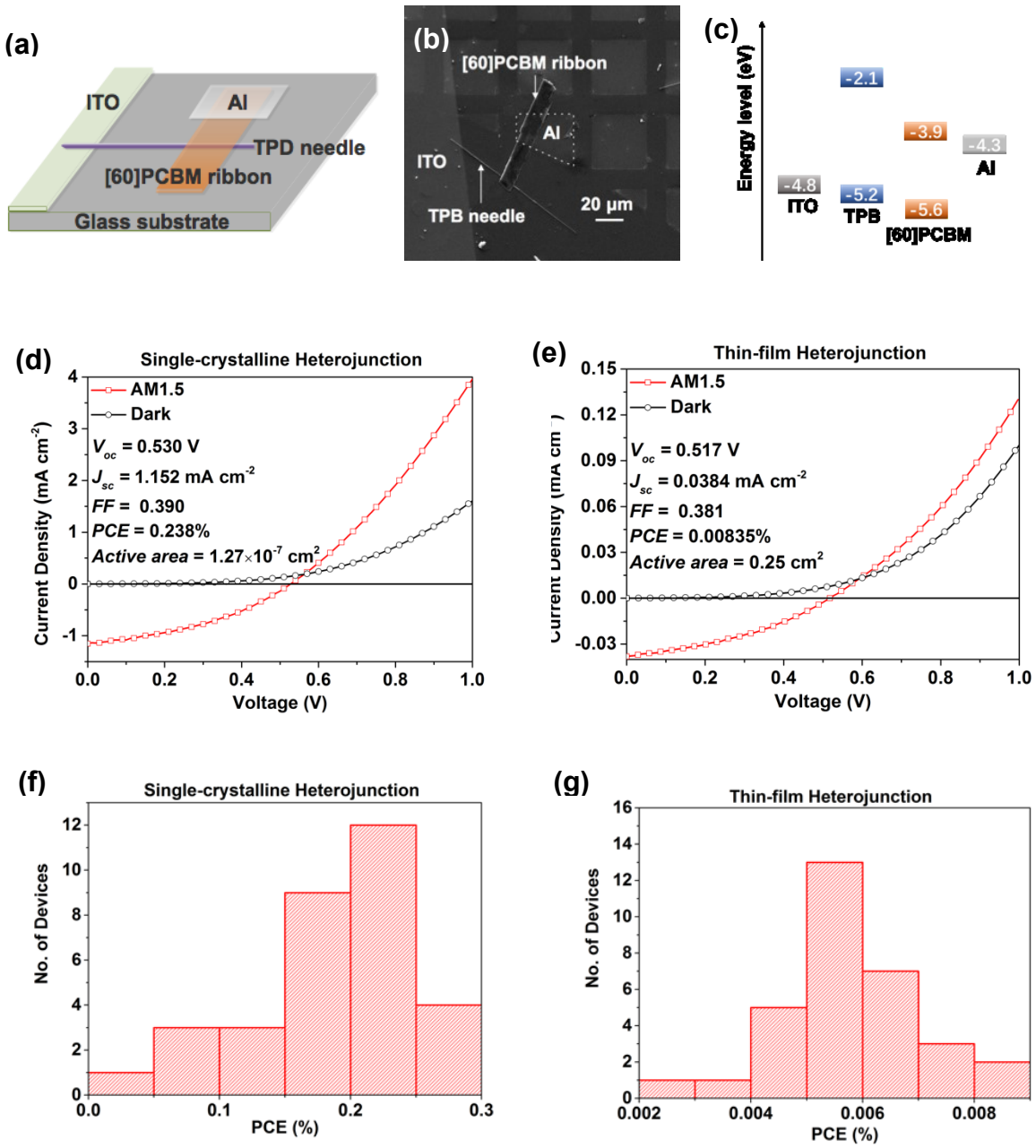

Figure 5 Solar cell performances of the single-crystalline and thin-film p-n heterojunctions. (a) Schematic configuration and (b) SEM image of the single-crystalline solar cell; (c) Energy level alignment of the device structures; Typical *J*–*V* curves of the (d) single-crystalline and (e) thin-film p-n heterojunction solar cells. Histogram of PCE values from (f) 32 single-crystalline devices and (g) 32 thin-film devices.

Table of contents entry

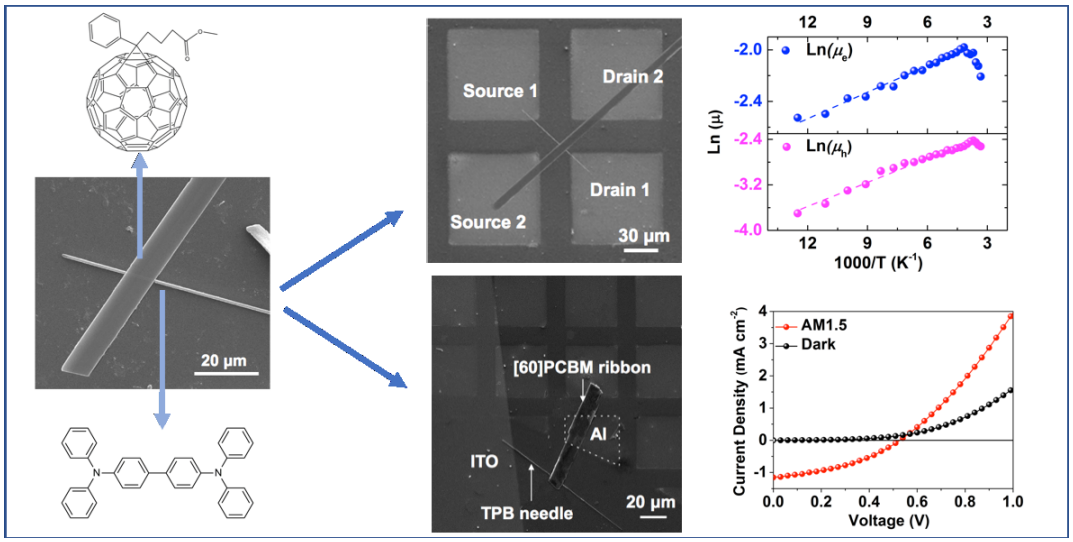

Solution-processed organic single-crystalline donor-acceptor heterojunctions (SCHJs) composed of N,N,N',N'-tetraphenylbenzidine (TPB) and phenyl-C_{61}-butyric acid methyl ester ([60]PCBM) were successfully obtained and fundamental studies on its charge transport properties were demonstrated; Revealing the advantages of applying single-crystalline heterojunctions in photovoltaic devices.

Keyword: Single-crystalline heterojunction; band-like; charge transport; organic photovoltaics

Xiaoming Zhao,‡ Tianjun Liu,‡ Yuteng Zhang, Shirong Wang, Xianggao Li, Yin Xiao, Xueyan Hou, Zilu Liu, Wenda Shi and T. John S. Dennis**

Organic Single-Crystalline Donor-Acceptor Heterojunctions with Ambipolar Band-Like Charge Transport for Photovoltaics